Tribology International 205 (2025) 110484

Contents lists available at ScienceDirect

Tribology International

journal homepage: www.elsevier.com/locate/triboint

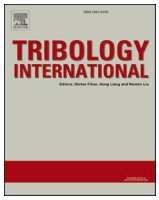

Oxide tribolayer breakdown on sliding metal contacts drives thermal ignition

Andres Garcia Jimenez [a], Timothy Wabel [b], Fabio A. Bendana [c], John D. DeSain [c], Levon Gevorkyan [b], Zachary C. Cordero [a,*]

[a] Aeronautics and Astronautics, Massachusetts Institute of Technology, Cambridge, MA 02090, United States
[b] Propulsion Department, The Aerospace Corporation, El Segundo, CA 90245, United States
[c] Propulsion Science Department, The Aerospace Corporation, El Segundo, CA 90245, United States

ARTICLE INFO

Keywords:
Metal combustion
Ignition
Tribolayer
Oxidational wear

ABSTRACT

Frictional heating at sliding metallic contacts in high-pressure oxygen environments can cause frictional ignition and metal fires. Alloys that resist frictional ignition tend to grow a thick, protective oxide tribolayer during sliding. Ignition occurs when this tribolayer breaks down, exposing the hot underlying metal to oxygen. This paper establishes a quantitative link between frictional ignition and tribolayer breakdown using thermal ignition theory. The tribolayer breakdown mechanisms that drive frictional ignition of several engineering alloys are determined experimentally. For the alloy Haynes 214, the dominant tribolayer breakdown mechanism transitions from melting of the underlying metal to mechanical failure as oxygen pressure decreases, demonstrating how operating conditions affect ignition behavior. Thermal ignition theory is used to determine a critical interfacial temperature above which an alloy ignites in the absence of an oxide tribolayer. For the alloys of present interest, this critical temperature is lower than both the interfacial temperature at ignition (when the tribolayer breaks down) and the alloy melting point. In the temperature range between the critical and ignition temperatures, the sliding contact is metastable, meaning ignition occurs if the tribolayer is disturbed. Ignition resistance can be improved by raising the critical temperature towards the alloy melting point through changes in component design, operating conditions, and material properties. Additionally, tailoring alloy chemistry to promote the growth of a breakdown-resistant tribolayer allows safe operation in the metastable regime.

1. Introduction

Oxygen-rich turbomachines expose materials to high-pressure oxygen, where frictional heating at sliding metallic contacts can trigger ignition and metal fires [1,2]. This risk is particularly severe in the oxygen-rich turbopumps of reusable staged-combustion rocket engines (e.g., Blue Origin's BE-4 and SpaceX's Raptor), which rely on sliding contacts in components like bearings, seals, and valves. Historically, studies on frictional ignition have focused on comparing the ignition resistance of materials under idealized test conditions [1-3]. These studies typically ranked materials based on the product of sliding speed and contact pressure at ignition. However, this metric is sensitive to variables such as oxygen pressure, loading rate, and contact geometry, limiting its utility for conditions outside those explicitly tested [4].

Recent work has shifted toward understanding the physical mechanisms driving frictional ignition to develop more general predictive models. A key insight is that ignition resistance depends on the structure, mechanical properties, and growth kinetics of the oxide tribolayer that forms during sliding [5–9]. This tribolayer protects the underlying metal from oxidation and lubricates the sliding interface, reducing frictional heating. Ignition occurs when the tribolayer breaks down, exposing the hot underlying metal to high-pressure oxygen. Our recent work identified several tribolayer breakdown mechanisms, with the dominant mode varying with test conditions [9]. For example, in Ni-Cr alloys, tribolayer breakdown due to metal melting occurs at higher oxygen pressure, while mechanical failure dominates at lower pressures. These findings highlight the role of operating conditions in ignition behavior, challenging the legacy approach to selecting oxygen-compatible materials based on a narrow set of test conditions.

Building on this background, the present study quantitatively links tribolayer breakdown to frictional ignition using thermal ignition theory. The core principle of thermal ignition theory is that ignition occurs

* Corresponding author.
E-mail address: zcordero@mit.edu (Z.C. Cordero).

https://doi.org/10.1016/j.triboint.2024.110484
Received 8 October 2024; Received in revised form 22 December 2024; Accepted 23 December 2024
Available online 25 December 2024

when the oxidative heat flux (q_{ox}) exceeds the heat dissipation rate (q_{loss}) [10–13],

$$q_{ox}(T) \geq q_{loss}(T). \quad (1)$$

Thermal ignition theory has been applied successfully in a range of contexts, including metal fires [10,12]. The critical temperature (T^*) is defined as the temperature at which the heat generation and dissipation rates are equal. Exceeding T^* results in uncontrolled oxidative heating. In sliding metal contacts, q_{ox} and q_{loss} depend on material properties, operating conditions, contact geometry, temperature, and the structure of the sliding interface. When a protective oxide tribolayer forms, it acts as a diffusion barrier, slowing oxidation kinetics, decreasing q_{ox}, and suppressing ignition. When the tribolayer breaks down, oxidation rates increase sharply, leading to thermal runaway and ignition.

This study uses thermal ignition theory to describe the frictional ignition behaviors of engineering alloys commonly used in high-pressure oxygen applications. Frictional ignition experiments on Monel 400, Monel K500, Toughmet 160, and Haynes 214 are used to assess their respective oxide tribolayer structures, mechanisms of tribolayer breakdown, and ignition temperatures. Complementary finite element simulations reveal the conditions under which Eq. (1) is satisfied in the absence of a tribolayer. Combining these results, we show that the critical temperature predicted by Eq. (1) provides a conservative lower bound for ignition temperature. In the presence of a tribolayer, the contact can operate above the critical temperature, in a metastable state where ignition occurs upon tribolayer breakdown. This analysis suggests strategies for optimizing material properties and operating conditions to increase the critical temperature and enhance ignition resistance. It also emphasizes the importance of tribolayer stability in developing ignition-resistant alloys. More broadly, the framework developed here provides a validated approach for designing robust sliding contacts in high-pressure oxygen systems.

2. Materials and methods

Frictional ignition experiments were performed using a specialized rig, described in detail in [9,14,15]. Tests were performed on four different engineering alloys – Monel 400 (M400), Monel K500 (MK500), Toughmet 160 (TS160), and Haynes 214 (H214). These materials were selected because of their wide range of compositions, mechanical properties, and ignition behaviors. The nominal compositions of these materials are summarized in Table 1.

Before testing, the cylindrical tube specimens were cleaned following ASTM 693–03 [16]. Ignition behaviors were assessed in dry O_2 environments, under oxygen pressures between 3.4 and 24.1 MPa. The shaft speed was 17,000 rpm, corresponding to a linear sliding speed of 22 m/s, and the contact pressure was ramped with time at 31 N/s, corresponding to 101 kPa/s. Ignition was detected by rapid excursions in either gas pressure or relative axial displacement between samples. At the end of each test, the samples were quickly separated, and the test chamber was purged with N_2.

Recovered specimens were characterized, with special attention to the microstructure at the rubbing interface. Specimens were inspected visually and using optical and electron microscopy. X-ray diffraction (XRD) using a Co x-ray source was used to identify phases at the rubbing interface. Non-ignited samples were mounted, cross-sectioned, mechanically polished, and imaged using scanning electron microscopy (SEM). Energy dispersive x-ray spectroscopy (EDS) was used to determine the phase distribution in the oxide tribolayer.

Thermochemical calculations were carried out using the FactSage free energy minimization software (with FTOxid, FactPS, and FSstel databases) [17] to corroborate EDS and x-ray phase identification, to generate phase-equilibria predominance diagrams, and to compute parameters (e.g., enthalpy of oxidation, oxide phase fractions, melting temperatures) relevant to the oxidation and ignition behaviors of each alloy.

3. Experimental results and discussion

3.1. Ni-Cu alloys

We assessed the frictional ignition behaviors of three cupronickel alloys – M400, MK500, and TS160. Fig. 1 shows measurements of their friction coefficient vs. time. At first contact, the friction coefficient is ~0.2, typical for metal/metal sliding contacts, then decays exponentially over ~20–30 s to a lower steady-state value, corresponding to the *in situ* growth of a lubricating oxide tribolayer. All materials, and TS160 especially, exhibit a sharp increase in friction coefficient prior to ignition. As described in [9], this behavior reflects tribolayer breakdown and the formation of metallurgical junctions.

Finite element simulations were carried out using COMSOL Multiphysics software [18] to compute the interfacial temperature at the rubbing surface [4]. The time-dependent friction coefficient used in the simulations was fitted to the experimental friction coefficient data of each material following the same procedure described in [9]. Fig. 2 shows the results of these interfacial temperature calculations for all three alloys. During the initial 10 s, there is a rapid rise in the interfacial temperature due to the initially high friction coefficient. Subsequently, the heating rate slows as the friction coefficient decays to a lower

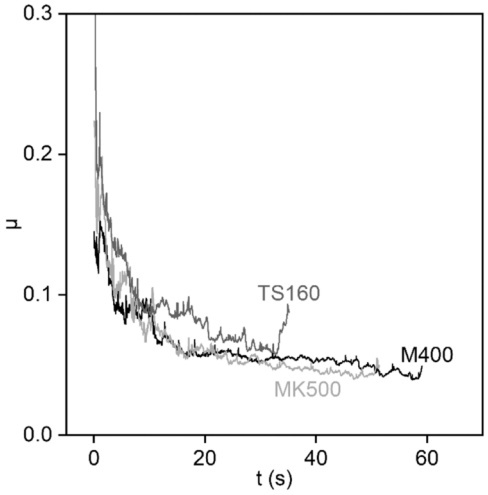

Fig. 1. Friction coefficient vs. time for M400, MK500, and TS160 under $PO_2 = 6.9$ MPa.

Table 1
Compositions of different materials tested.

Alloy	Composition (wt%)														
	Ni	Cu	Cr	Al	C	Co	Fe	Mn	Mo	Nb	Si	Sn	Ti	W	Zr
M400	65.2	30			0.3		2.5	2			0.5				
MK500	62.2	30		3	0.25		2	1.5			0.5		0.5		
TS160	15	77										8			
H214	72.2		16	4.5	0.04	2	3	0.5	0.5	0.15	0.2		0.5	0.5	0.1

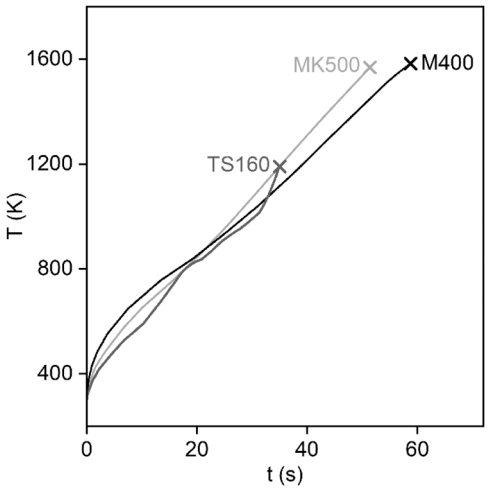

Fig. 2. Calculated interfacial temperature vs. time for M400, MK500, and TS160 under $PO_2 = 6.9$ MPa.

steady-state value and heat diffuses from the rubbing surface. The ignition temperatures of M400, MK500, and TS160 are 1580 K, 1550 K, and 1190 K, respectively. Comparing the interfacial temperature vs. time curves of M400 and MK500 in Fig. 2 reveals the effects of material properties on ignition behaviors. We observe that while both materials ignited at similar temperatures, MK500 ignited ~8 s earlier than M400. The shorter ignition time of MK500 is due to its lower thermal conductivity (18 $Wm^{-1}K^{-1}$ for MK500 vs. 22 $Wm^{-1}K^{-1}$ for M400), which traps heat at the rubbing surface and accelerates the interfacial temperature rise.

3.1.1. Ignition mechanisms of Monel 400 and Monel K500

Fig. 3 shows an SEM micrograph of the oxide tribolayer formed on M400 from a test interrupted at 59 s, just prior to expected ignition. XRD results shown in Fig. 4 indicate that the main phases in the tribolayer are NiO and Cu_2O. EDS mapping was used to determine the phase distribution in the tribolayer, which agrees with XRD results, revealing a dense outer layer of equiaxed NiO grains surrounded by Cu_2O. The spatial distribution and morphology of the NiO and Cu_2O phases are consistent with molten Cu_2O wetting the grain boundaries of the more refractory NiO phase. This is in line with a predicted peak interfacial temperature ~20 K higher than the melting point of Cu_2O (1520 K). This outer layer covers a porous inner layer of NiO and a metallic Cu-Ni solid solution. Stereological measurements showed that the top layer consists of 75 vol% NiO and 25 vol% Cu_2O, while the layer closer to the metal interface contains 70 vol% NiO and 30 vol% Ni-Cu solid solution.

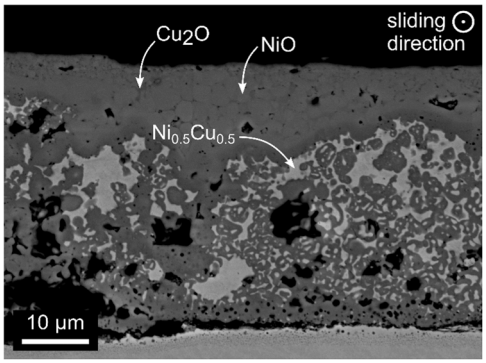

Fig. 3. SEM micrograph of the M400 tribolayer formed during frictional ignition under $PO_2 = 6.9$ MPa. The peak interfacial temperature (T_p) was 1540 K and test duration (t_s) was 59 s.

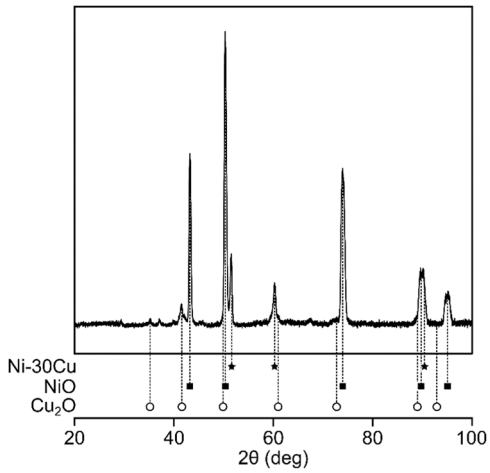

Fig. 4. XRD pattern from the M400 tribolayer. Data was collected using a Co x-ray source.

Thermochemical calculations were used to develop the PO_2-temperature predominance diagram for M400 shown in Fig. 5. The broken lines in Fig. 5 indicate the interfacial temperatures in the interrupted experiment (black) and at ignition (red). We computed the temperature drop across the oxide in the interrupted experiment using the linearized heat flux equation

$$\Delta T = \frac{q}{k_{ox}} L_{ox}, \tag{2}$$

where L_{ox} is the oxide thickness (40 μm) and k_{ox} is the thermal conductivity of the oxide, estimated as the volume average thermal conductivity of the different phases – 96 $Wm^{-1}K^{-1}$ [19–21]. q is the frictional heat flux, given by

$$q = \mu P v, \tag{3}$$

where μ is the friction coefficient, P is the contact pressure, and v is the sliding speed. Based on the thickness of the oxide tribolayer we estimate a temperature drop of ~40 K across the oxide scale in the interrupted experiment.

The phase diagram predicts that at the peak interfacial temperature of 1540 K the oxide tribolayer should comprise three layers – an outer

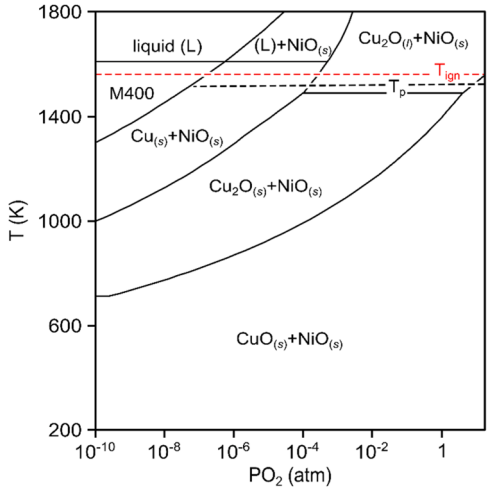

Fig. 5. Predominance diagram for M400. The black broken line indicates the temperature profile across the oxide tribolayer on the specimen from the interrupted experiment (cf. Fig. 3). The red broken line indicates the calculated ignition temperature under $PO_2 = 6.9$ MPa.

layer with 63 vol% NiO and 37 vol% CuO; a middle layer of 65 vol% NiO and 35 vol% Cu_2O; and an inner layer at the metal/oxide interface of 73 vol% NiO and 27 vol% metallic Cu. Stereological measurements of the phase volume fractions match the thermochemical predictions with the exception of the NiO-CuO outer layer. We do not observe CuO in the tribolayer likely because CuO can only support a small chemical potential gradient, resulting in a thin outer layer of NiO and CuO that wears off during sliding.

The good agreement between the phase distribution of the oxide tribolayer and that predicted at equilibrium likely stems from the short duration of the frictional ignition experiments, which prevents long-range cation diffusion, effectively suppressing microstructural evolution processes that dominate under long-duration static oxidation experiments [22–25]. We can show this quantitatively by comparing the tribolayer dimensions with the diffusion distance (Δx) of Ni cations during a frictional ignition experiment, estimated using

$$\Delta x \approx \int_0^{t_s} \frac{1}{2}\sqrt{\frac{D_{eff}}{t}}dt, \tag{4}$$

where t_s is the test duration and D_{eff} is the effective diffusivity of Ni cations in polycrystalline NiO [26],

$$D_{eff} = 6.4\left(D_L + \frac{2(D_{GB}\delta)}{g}\right). \tag{5}$$

This effective diffusivity expression includes contributions from lattice diffusion ($D_L = 5.0\times 10^{-2}\exp\left(\frac{-200\ \text{kJ/mol}}{RT}\right)$ m^2/s) and short-circuit diffusion along grain boundaries ($D_{GB} = 7.6\times 10^{-5}\exp\left(\frac{-170\ \text{kJ/mol}}{RT}\right)$ m^2/s) [26–28], where δ is the grain boundary width (0.5 nm), and g is the average grain size of the oxide, determined experimentally to be 5 μm. Considering the interfacial temperature rise during the M400 experiment, Eq. (4) predicts a net cation diffusion distance of only 15 μm, which is a fraction of the oxide tribolayer thickness of 40 μm, confirming a lack of long-range diffusion.

In the predominance diagram in Fig. 5, the frictional ignition temperature of M400 (1580 K) lies between the melting points of the underlying metal (1640 K) and Cu_2O (1520 K), indicating that prior to ignition the oxide melts and sloughs off, exposing the hot underlying metal to high-pressure oxygen and triggering metal ignition. While melting of the underlying metal may also contribute to tribolayer breakdown, the lower melting point of Cu_2O provides a conservative bound on the ignition temperature of M400.

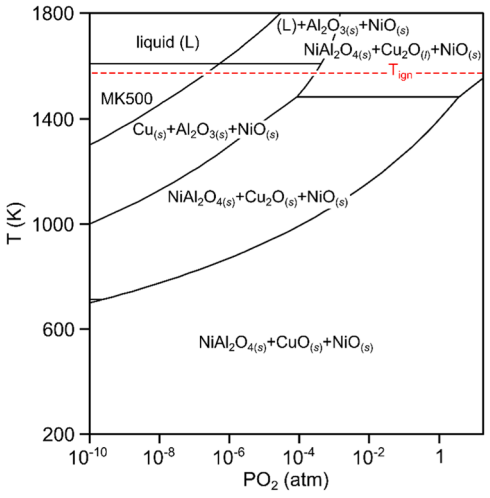

Fig. 6. Predominance diagram for MK500. The red broken line indicates the calculated ignition temperature under $PO_2 = 6.9$ MPa.

Fig. 6 is a predominance diagram for MK500, indicating that at the oxide/gas interface a CuO, NiO, and $NiAl_2O_4$ layer forms, followed by an interlayer of Cu_2O, NiO, and $NiAl_2O_4$. At the oxide/metal interface a layer of NiO, Al_2O_3, and metallic Cu forms. The red broken line in Fig. 6 indicates the ignition temperature under PO_2 of 6.9 MPa. As in M400, the ignition temperature of MK500 (1550 K) lies between the melting point of the alloy (1650 K) and the melting point of Cu_2O (1520 K). Accordingly, MK500 also ignites from melting of an oxide constituent in the tribolayer.

3.1.2. Ignition mechanisms of TS160

Fig. 7 shows an SEM micrograph of the 38 μm thick oxide tribolayer formed on TS160. The XRD pattern in Fig. 8 indicates that the main phases in the tribolayer are NiO, CuO, Cu_2O, and SnO_2. EDS mapping of the oxide tribolayer agrees with the XRD results, revealing a bilayer structure with an outer layer of CuO, NiO, and micron-sized SnO_2 particles, followed by an inner layer at the oxide/metal interface composed of Cu_2O and NiO with nanoscale SnO_2 inclusions. There was no microstructural evidence of melting in either the oxide or underlying metal. The tribolayer shows signs of extensive plastic deformation, including a fine grain structure in the underlying metal near the metal/oxide interface, which formed through dynamic recrystallization, and large oxide inclusions in the underlying metal, which resulted from mechanical mixing. Finally, we also observe pores in the metal close to the metal/oxide interface which likely result from cation vacancy condensation during rapid oxidation.

Fig. 9 shows the O_2 pressure-temperature predominance diagram for TS160. The black broken line indicates the temperature across the oxide tribolayer in the interrupted experiment. In this case the temperature drop across the tribolayer was ~8 K. The predominance diagram shows that a CuO, NiO, and SnO_2 layer forms closer to the oxide/gas interface, followed by an interlayer of Cu_2O, NiO, and SnO_2. Finally, a layer of NiO, SnO_2, and metallic Cu forms at the metal/oxide interface. Similar to the M400 tribolayer, the TS160 tribolayer is essentially a snapshot of the phase diagram at the interfacial temperature, providing further confidence in using equilibrium thermochemical calculations to predict the oxide phases in tribolayers formed during frictional ignition.

The TS160 predominance diagram also shows the interfacial temperature at ignition (red broken line; 1190 K) which corresponds to the melting point of TS160 (1200 K) and is lower than the melting point of any of the oxide phases in the tribolayer. This direct correlation between melting of the underlying metal with the onset of frictional ignition indicates that tribolayer breakdown in TS160 also occurs via a melt-driven mechanism. However, instead of oxide melting as in M400, in TS160 the underlying metal melts, disrupting the oxide tribolayer, exposing the hot underlying metal to high-pressure oxygen, and triggering ignition. Comparing the ignition behaviors of TS160, MK500, and

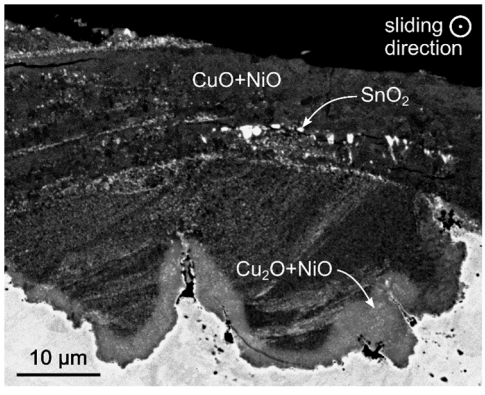

Fig. 7. SEM micrograph of the TS160 tribolayer formed during frictional ignition. The peak interfacial temperature (T_p) was 890 K and test duration (t_s) was 30 s.

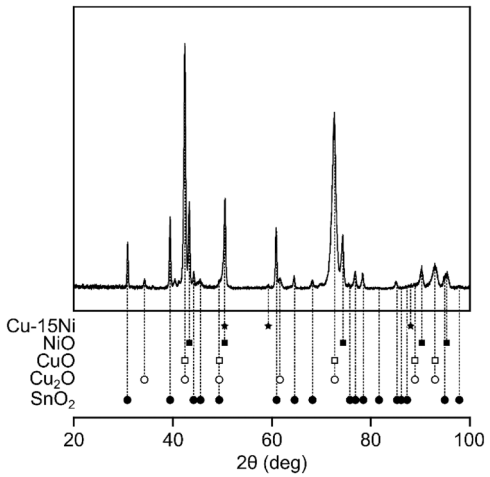

Fig. 8. XRD pattern from the TS160 tribolayer. Data was collected using a Co x-ray source.

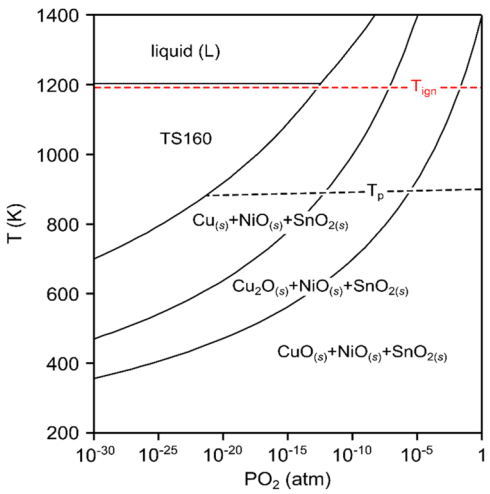

Fig. 9. Predominance diagram for TS160. The black broken line indicates the temperature drop across the oxide tribolayer in the interrupted experiment (see Fig. 7). The red broken line indicates the calculated ignition temperature under $PO_2 = 6.9$ MPa.

M400 highlights the effects of material chemistry on ignition resistance. A higher Cu concentration and the addition of low melting point Sn degrades the ignition resistance of TS160 by lowering the melting point (i.e., the ignition temperature) by ~400 K and decreasing the ignition time by roughly half.

3.1.3. *Effects of oxygen pressure on frictional ignition behaviors*

Frictional ignition experiments on M400 and MK500 were performed under oxygen pressures ranging from 6.9 to 24.2 MPa. The steady-state friction coefficient shown in Fig. 10a as well as the magnitude and the form of the friction coefficient vs. time curves were the same under all O_2 pressures, indicating that the sliding behavior of the Monel alloys is insensitive to PO_2 within the range of pressures considered in this study. The ignition temperatures were calculated using the friction coefficient and the FEM described in [4,9], which included the effects of pressure on the thermal properties of O_2 gas reported in the open literature [29–32]. Fig. 10b shows the ignition temperature vs. PO_2 for both M400 and MK500. The ignition temperatures are similar under all oxygen pressures and correspond to the melting point of Cu_2O, suggesting that the ignition mechanism of both alloys is insensitive to PO_2 and continues to be driven by melting of the oxide tribolayer. The ignition time vs. PO_2

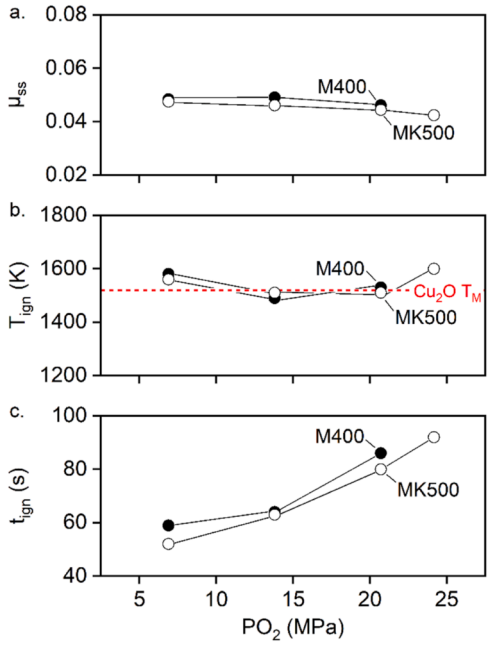

Fig. 10. (a) Steady-state friction coefficient vs. PO_2; (b) ignition temperature vs. PO_2; and (c) ignition time vs. PO_2 for M400 and MK500. The red broken line indicates the melting point of the Cu_2O oxide phase.

shown in Fig. 10c indicates that the ignition time increases with PO_2 for both M400 and MK500. The delayed ignition times are due to the increase in convection from the sample to the surrounding gas with higher PO_2, which helps dissipate heat from the rubbing interface. Accordingly, for Ni-Cu alloys higher oxygen pressures do not necessarily promote ignition.

3.1.4. *Key frictional ignition behaviors of Ni-Cu alloys*

The present results establish the good agreement between the phase distribution observed in the tribolayers and that predicted by equilibrium thermochemical calculations, indicating that equilibrium calculations can accurately predict phases in oxide tribolayers. They also demonstrate the direct link between tribolayer breakdown and frictional ignition. M400 and MK500 ignite due to melting of the oxide tribolayer whereas TS160 ignites due to melting of the underlying metal. Accordingly, in melt-driven frictional ignition, the dominant ignition mechanism (oxide melting vs. metal melting) is determined by whichever has the lower melting point.

The sliding behavior of M400 and MK500 is insensitive to PO_2 as the form of the friction coefficient curve and the magnitude of the steady-state friction coefficient are consistent under all O_2 pressures. Similarly, the ignition mechanism – melting of the oxide tribolayer – remains the same under all O_2 pressures (i.e., the ignition temperature is insensitive to PO_2). However, under higher PO_2 the ignition times are delayed because more heat is dissipated into the surrounding O_2 gas, suggesting that for Ni-Cu alloys a higher O_2 pressure does not necessarily translate to an increased risk of ignition.

From Fig. 10b and c we also observe that under all test conditions, MK500 and M400 have similar ignition behaviors – similar ignition times and identical ignition temperatures – despite their different chemistry. MK500 contains Al and Ti, reactive elements that enhance strength and hardness but generally degrade burn resistance. These results have implications for the design of ignition-resistant alloys suggesting that Al, Ti, and other reactive alloying elements used to improve mechanical properties can be added in minor concentrations to alloys without significantly compromising ignition resistance.

3.2. Ni-Cr alloy: Haynes 214

Frictional ignition experiments on H214 were performed under PO_2 of 3.4 and 6.9 MPa. The form of the friction coefficient vs. time curves shown in Fig. 11 and the magnitude of the steady-state friction coefficient are the same under both oxygen pressures, indicating that the friction coefficient is insensitive to PO_2 over the range of pressures tested. The interfacial temperature vs. time under both O_2 pressures shown in Fig. 12 was calculated using the friction coefficient shown in Fig. 11. As in our previous results on the ignition behavior of Ni-20Cr [9], under a PO_2 of 3.4 MPa H214 ignites in roughly half the time (42 s) compared to the test under PO_2 of 6.9 MPa, which ignited in 110 s. Under PO_2 of 3.4 MPa the H214 ignition temperature is 1430 K, roughly 200 K lower than the ignition temperature under PO_2 of 6.9 MPa (1650 K). Interestingly, while H214 has a higher strength relative to Ni-20Cr, it ignites at a similar temperature (1650 K vs. 1630 K for Ni-20Cr [9]) and time (110 s vs. 115 s for Ni-20Cr [9]), suggesting that decreasing the Cr content (20 wt% in Ni-20Cr vs. 16 wt% in H214) and adding strengthening alloying elements, Al and Ti, in H124 has a negligible effect on ignition resistance. However, examination of recovered samples revealed that once ignited, the H214 samples suffered greater damage than Ni-20Cr samples, indicating that these reactive elements (e.g., Al, Ti) may significantly degrade the burn resistance of H214. These results point towards an optimal concentration of reactive alloying elements that can enhance mechanical properties without jeopardizing ignition and burn resistance.

Fig. 13 is a micrograph of the oxide tribolayer on H214. The tribolayer exhibits through-thickness channels cracks and cracks parallel to the oxide/metal interface. The channel cracks result from high thermal stresses, high contact pressures, and incompatible deformation between the brittle oxide tribolayer and ductile underlying metal. Cracks parallel to the oxide/metal interface are observed more prominently at the interface between the interlayers of different oxide phases. These parallel cracks result from buckling delamination due to compressive stresses during cooling at test shutdown.

Fig. 14 shows a high-magnification SEM image of the boxed region in Fig. 13. Initial observation reveals an oxide tribolayer with a complex phase morphology and an average thickness of 100 μm. XRD results in Fig. 15 show that the main phases in the oxide tribolayer are NiO and $NiCr_2O_4$. Static oxidation experiments of Ni-Cr-Al alloys with similar composition (Ni-17Cr-9Al, wt%) as H214 developed overlayers composed mainly of NiO, $Ni(Al,Cr)_2O_4$, and $(Al,Cr)_2O_3$ [33–35]. We do not observe $NiAl_2O_4$ and $(Al,Cr)_2O_3$ in our XRD analysis likely because the x-rays were unable to penetrate the thick tribolayer and resolve

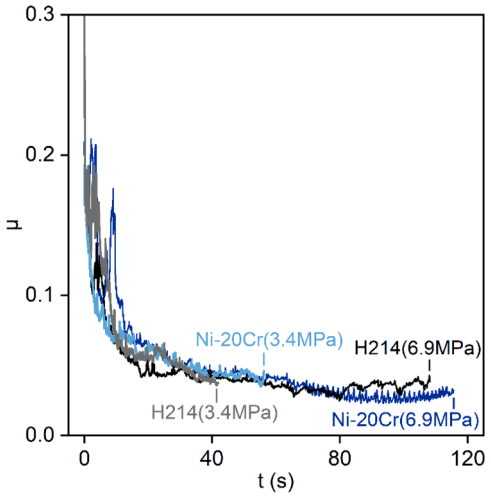

Fig. 11. Friction coefficient vs. time for H214 and Ni-20Cr under $PO_2 = 3.4$ and 6.9 MPa. Ni-20Cr data from [9] is included for comparison.

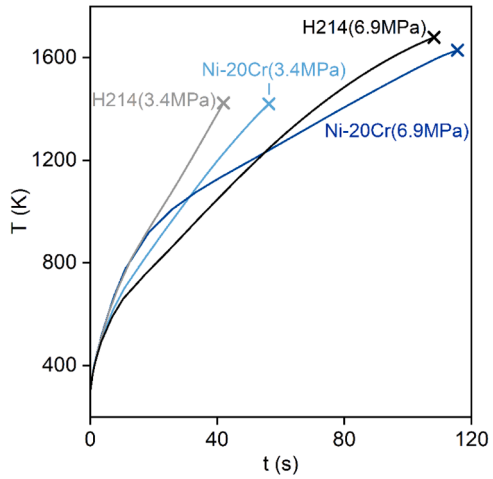

Fig. 12. Calculated interfacial temperature vs. time for H214 and Ni-20Cr under $PO_2 = 3.4$ and 6.9 MPa. Ni-20Cr data from [9] is included for comparison.

phases with lower volume fractions. EDS mapping of Fig. 14 indicates that the structure of the H214 tribolayer consists of a 20 μm thick outer layer of micron-scale NiO grains decorated with nanoscale $NiCr_2O_4$ precipitates. The NiO and $NiCr_2O_4$ layer is followed by an interlayer with a complex phase structure composed of Al_2O_3, NiO, $Ni(Al,Cr)_2O_4$, and nanoscale metallic Ni particles. We refer to this region as the Al-Cr-Ni oxide interlayer. At the oxide/metal interface, we observe a 1 μm thick layer of $(Al,Cr)_2O_3$. Porosity is observed in the $NiCr_2O_4$ and NiO layer as well as in the Al-Cr-Ni oxide interlayer, with larger pores located closer to the $(Al,Cr)_2O_3$ interlayer. There are no microstructural signs of melting in either the oxide or underlying metal.

Fig. 16 shows the equilibrium predominance diagram of H214. The predominance diagram predicts that at the oxide/gas interface, a NiO and $Ni(Cr,Al)_2O_4$ layer forms, followed by an interlayer of $Ni(Cr,Al)_2O_4$ and metallic Ni. This interlayer is followed by a layer of $Ni(Cr,Al)_2O_4$, $(Al,Cr)_2O_3$, and metallic Ni. Finally, at the metal/oxide interface a layer of Cr_2O_3 and Al_2O_3 with metallic Ni forms. While the complexity of the Al-Cr-Ni oxide interlayer observed in Fig. 14 is not captured by the phase diagram, there is substantial agreement between the predicted phases from equilibrium thermochemical calculations with those observed in the tribolayer. The phase diagram also shows the temperature drop of 30 K across the tribolayer on the recovered non-ignited sample tested under PO_2 of 6.9 MPa, which is indicated by the black broken line. The ignition temperature under both O_2 pressures is also indicated by the red broken lines in Fig. 16. The peak temperature in the recovered non-ignited sample is below the ignition temperature. As in Ni-20Cr [9] and TS160, the ignition temperature of H214 under PO_2 of 6.9 MPa corresponds to the melting point of the alloy, indicating that tribolayer breakdown in H214 results from melting of the underlying metal. Under the lower PO_2 of 3.4 MPa, the ignition temperature is ~180 K lower than the melting point of the alloy.

A possible explanation for the lower ignition temperature under PO_2 of 3.4 MPa is localized flash heating at asperity contacts that causes the local asperity temperature to reach the alloy melting point. Using the modified flash heating model described in [9], we estimated that the final temperature including flash heating effects was 1460 K under PO_2 of 3.4 MPa, which is still ~150 K lower than the melting point of H214. This same behavior was observed on Ni-20Cr under a PO_2 of 3.4 MPa (cf. Fig. 12), suggesting that as in Ni-20Cr there is a transition in the dominant ignition mechanism of H214 from melt-driven under a PO_2 of 6.9 MPa to solid-state mechanically-driven tribolayer breakdown under a PO_2 of 3.4 MPa.

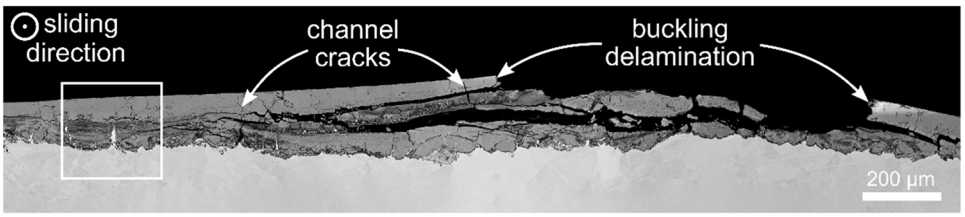

Fig. 13. Macrograph of the H214 tribolayer. The boxed region corresponds to the micrograph in Fig. 14. The peak interfacial temperature (T_p) was 1630 K and test duration (t_s) was 121 s.

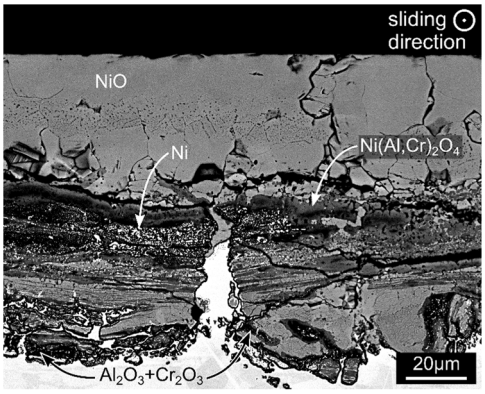

Fig. 14. SEM micrograph of the H214 tribolayer formed during frictional ignition. Micrograph is a high-magnification image of the boxed region in Fig. 13. The peak interfacial temperature (T_p) was 1630 K and test duration (t_s) was 121 s.

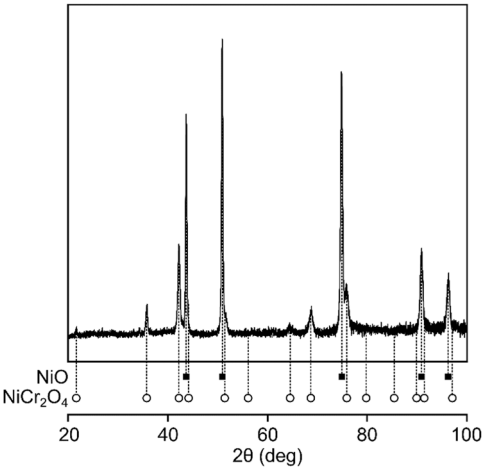

Fig. 15. XRD pattern from the H214 tribolayer. Data was collected using a Co x-ray source.

4. Melt-driven vs. solid-state mechanically-driven frictional ignition

For most engineering alloys, the melting point of the metal is significantly lower than those of its corresponding oxide phases, suggesting that melt-driven ignition will typically result from melting of the underlying metal. Fig. 17 compares the frictional ignition temperatures and melting points of several alloys under PO_2 of 6.9 MPa. Frictional ignition temperatures for alloys not included in this study were calculated using published data from previous frictional ignition experiments [1,2]. In Fig. 17 we observe that several alloys (H214, Ni-20Cr, Nickel 200, and others) have frictional ignition temperatures close to their melting points, indicating that these materials ignite via a melt-driven

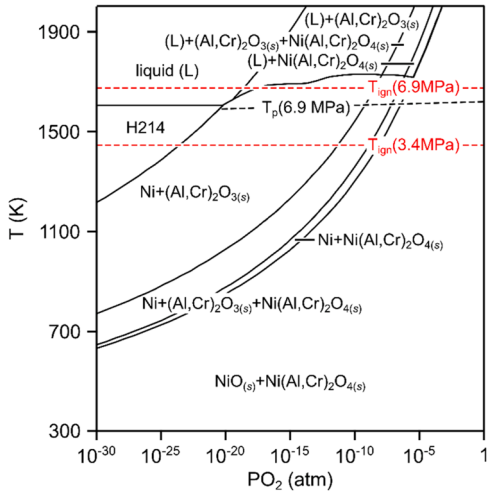

Fig. 16. Predominance diagram for H214. The black broken line indicates the temperature across the oxide tribolayer in the interrupted experiment. The red broken lines indicate the calculated ignition temperature under PO_2 of 6.9 and 3.4 MPa.

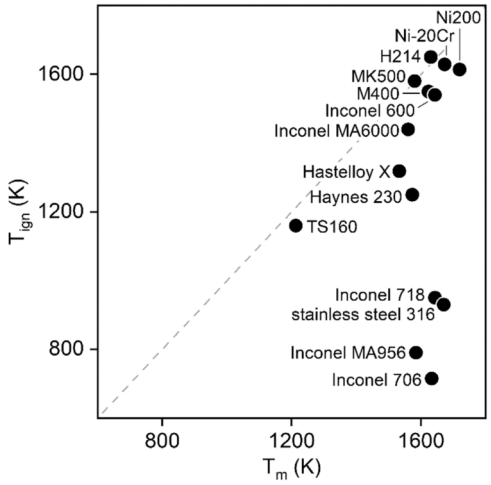

Fig. 17. Frictional ignition temperature vs. melting point for select alloys under PO_2 = 6.9 MPa [1,2,4]. Alloys with high Fe content have a larger discrepancy between their melting points and frictional ignition temperatures.

mechanism. For other alloys (e.g., Inconel 718, stainless steel 316, Hastelloy X, Inconel 600, and others) frictional ignition temperatures are appreciably lower than their melting point and the melting points of any of their oxides. The difference between the melting points and the frictional ignition temperatures is approximately 100 K and 220 K for Inconel 600 and Hastelloy X, respectively, and increases to ~740 K for stainless steel 316, which has a melting point of 1670 K and a frictional ignition temperature of 930 K [4]. The difference between the melting

points and frictional ignition temperatures scales with Fe content, with Inconel 600, Hastelloy X, and stainless steel 316, having progressively higher Fe content and a correspondingly larger difference between their melting points and frictional ignition temperatures. Others have also pointed to a connection between higher Fe content and lower ignition and combustion resistance as assessed through frictional ignition and promoted combustion testing [1,36–38].

Flash heating at asperity contacts cannot explain the discrepancy between the melting points and frictional ignition temperatures. For example, accounting for flash heating effects, the final interfacial temperature of stainless steel 316 is estimated to be 970 K, still 700 K below the melting point. Consequently, similar to the ignition of H214 and Ni-20Cr under PO_2 of 3.4 MPa, the alloys in Fig. 17 that have ignition temperatures below their melting points likely ignite due to mechanical failure of the oxide tribolayer. The results in Fig. 17 also indicate that the assumption that metals ignite when they melt (i.e., ignition temperature corresponds to melting point of the alloy) is non-conservative because only a few select alloys ignite via a melt-driven mechanism.

5. Criterion for thermal ignition

From thermal ignition theory, ignition sets on when Eq. (1) is satisfied, i.e., the heat generation rate from oxidation exceeds the heat dissipation rate. We can further understand the experimental results above in the context of this ignition criterion by considering oxidation rates during tribolayer growth and after tribolayer breakdown, which represent the two limiting cases of heat generation – i.e., in the presence or in the absence of an oxide diffusion barrier. This analysis reveals the effects of material properties (e.g., tribolayer structure, melting points, enthalpy of oxidation) and design variables (e.g., component geometry, oxygen pressure) on the likelihood of frictional ignition.

5.1. Rate of heat generation from oxidation

During oxidation, the heat generation rate (q_{ox}) is

$$q_{ox} = \frac{H_{ox}}{M_m}\frac{dm_c}{dt}, \tag{6}$$

where M_m is the molar mass of the metal, H_{ox} is the enthalpy of oxidation per unit mole of metal, and m_c is the mass of metal consumed during oxidation per unit area. When an oxide tribolayer forms, oxidation kinetics slow down because the tribolayer serves as a diffusion barrier that inhibits further oxidation. In this case, we assume parabolic oxidation kinetics such that the rate of metal consumption depends on the instantaneous mass of the metal consumed ($m_{c,diff}$) and has an Arrhenius temperature dependence,

$$\frac{dm_{c,diff}}{dt} = \left(\frac{M_m}{M_{O_2}}\beta\right)^2\left(A_{diff}e^{-\frac{Q_{diff}}{RT}}\right)\frac{1}{m_{c,diff}} = \left(\frac{\rho_{ox}}{\gamma}\frac{M_m}{M_{ox}}\right)^2\frac{dL_{ox}}{dt}\frac{L_{ox}}{m_{c,diff}}, \tag{7}$$

where R is the gas constant, M_{O_2} is the molar mass of O_2 gas, and β is the ratio of moles of metal to moles of oxygen consumed, computed using equilibrium thermochemical calculations. In Eq. (7), the prefactor A_{diff} and the activation energy Q_{diff} depend on material chemistry. The rate of metal consumption (see Eq. (7)) is also written in terms of the oxide growth rate (dL_{ox}/dt), where L_{ox} is the instantaneous oxide thickness, ρ_{ox} is the average density of the oxide tribolayer, M_{ox} is the average molar mass of the oxide tribolayer, and γ is the ratio of moles of oxide formed to moles of metal consumed computed using equilibrium thermochemical calculations.

Quinn [39–41] and others [42,43] have established that oxide growth kinetics are much faster during high-speed sliding than in conventional static oxidation experiments. Similarly, in our previous work on frictional ignition of Ni-Cr alloys, we observed that oxide tribolayers grew orders of magnitude faster than oxide overlayers grown under similar temperatures in static oxidation tests [9]. Accordingly, we use the results from frictional ignition experiments, temperature calculations from the FEM, and equilibrium thermochemical calculations to calibrate the values of A_{diff} and Q_{diff} for oxide growth during sliding. For a given pair of A_{diff} and Q_{diff}, we numerically integrate Eq. (7) over the time range of the non-ignited frictional ignition experiment to estimate a final tribolayer thickness. We then compare the predicted tribolayer thickness with that measured on recovered non-ignited samples. This process is repeated for different combinations of A_{diff} and Q_{diff} until the predicted oxide thickness converges to the experimentally measured value. The calibrated values of A_{diff} and Q_{diff} for each of the materials in this study are included in Table 2.

Table 2
Calibrated values for oxidation kinetics.

Alloy	A_{diff} ($kg^2m^{-4}s^{-1}$)	Q_{diff} (kJ/mol)
Monel 400	100	165
Toughmet 160	595	110
Haynes 214	169	170

Substituting Eq. (7) into Eq. (6) we obtain the heat generation rate from oxidation in the presence of an oxide tribolayer,

$$q_{ox,diff} = \frac{H_{ox}M_m}{m_{c,diff}}\left(\frac{\beta}{M_{O_2}}\right)^2\left(A_{diff}e^{-\frac{Q_{diff}}{RT}}\right). \tag{8}$$

The enthalpy of oxidation varies with temperature, as shown in Fig. 18 for M400, TS160, and H214. For all materials the enthalpy of oxidation decreases with temperature because the enthalpy of the alloy rises faster than that of the oxide products, resulting in a net reduction in the enthalpy of oxidation. In Fig. 18 the enthalpy of oxidation of M400 has a kink at 1520 K due to melting of Cu_2O.

Breakdown of the tribolayer eliminates the diffusion barrier and accelerates the oxidation rate, resulting in a new form of q_{ox}. Assuming the oxidation rate is limited by oxygen adsorption on a virgin metal surface, the rate of metal consumption ($m_{c,ad}$) can be approximated as

$$\frac{dm_{c,ad}}{dt} = \left(\frac{M_m}{M_{O_2}}\beta\right)\left(A_{ad}e^{-\frac{Q_{ad}}{RT}}\right). \tag{9}$$

In Eq. (9), the activation energy Q_{ad} is taken to be ~100 kJ/mol, a typical value for oxygen adsorption on metal surfaces [44–47], and the

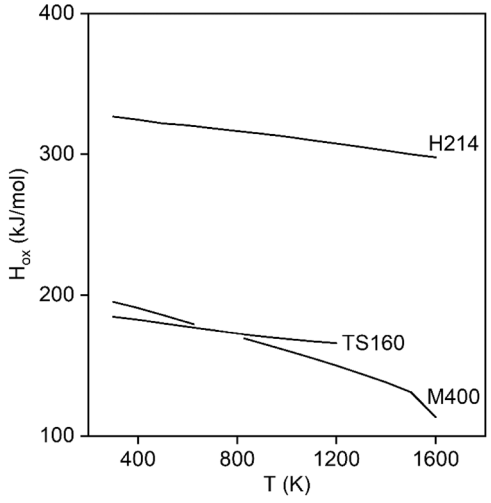

Fig. 18. Enthalpy of oxidation vs. temperature for M400, TS160, and H214 under $PO_2 = 6.9$ MPa based on equilibrium thermochemical calculations, performed using FactSage [17].

prefactor A_{ad} is given by the Hertz-Knudsen equation for surface adsorption of gas molecules [48,49],

$$A_{ad} = \alpha P_g \sqrt{\frac{M_{O_2}}{2\pi R T_0}}, \tag{10}$$

where P_g is the gas pressure and α is a sticking coefficient taken to be unity. In evaluating Eq. (9), we assume that P_g is the pressure of the O_2 gas and T_0 is the ambient temperature. Combining Eqs. (6), (9), and (10), yields the heat generation rate from oxidation under adsorption ($q_{ox,ad}$), i.e., when the tribolayer is absent,

$$q_{ox,ad} = \frac{H_{ox}\beta\alpha P_g}{\sqrt{2\pi M_{O_2} R T_0}} e^{-\frac{Q_{ad}}{RT}}. \tag{11}$$

In the following analysis we evaluate Eqs. (8) and (11) for M400, TS160, and H214 using the present experimental results, equilibrium thermochemical calculations, and the calculated interfacial temperatures.

5.2. Rate of heat dissipation

We also consider the heat dissipation rate from the sliding surface (q_{loss}) by assuming that heat dissipates via conduction (q_{cond}), radiation (q_{rad}), and convection (q_{conv}). The total heat dissipation rate is the sum of each of these contributions,

$$q_{loss} = q_{cond} + q_{rad} + q_{conv}. \tag{12}$$

This expression depends on material properties and system parameters such as O_2 pressure and component geometry. Different sliding contacts and specimen geometries will result in different heat dissipation rates. In our sample geometry, the walls of the tubular sample are thin compared to its axial length, thus we assume 1-D heat transfer only in the axial direction such that the temperature remains uniform across the thickness of the sample wall. Using Fourier's law, the contribution of heat dissipation due to conduction is

$$q_{cond} = \kappa_m \left.\frac{\partial T}{\partial x}\right|_{x_s}, \tag{13}$$

where κ_m is the temperature-dependent thermal conductivity of the alloy. The temperature gradient in Eq. (13) is evaluated at the rubbing interface (x_s) and calculated numerically using the temperature distribution along the sample from FEM. The heat dissipated due to radiation is computed using Stefan-Boltzmann law,

$$q_{rad} = \epsilon\sigma_B\left(T^4 - T_0^4\right), \tag{14}$$

where σ_B is the Stefan-Boltzmann constant, ε is the emissivity of the alloy taken to be constant and equal to 0.5, T_0 is cold wall temperature, and T is the surface temperature calculated using FEM. Finally, we compute the heat dissipation due to convection assuming Newton's law of cooling,

$$q_{conv} = h(T - T_0), \tag{15}$$

where h is the convective heat transfer coefficient determined using the Anderson et al. correlation [50] for a cylinder rotating along its longitudinal axis in still air,

$$h = 0.07\left(D\omega^2 \frac{C_p \eta \kappa_{O_2}^2}{\nu^2}\right)^{1/3}. \tag{16}$$

In Eq. (16) D is the outer diameter of the sample, ω is the angular speed of the rotor (1700 rad/s), C_p is the specific heat capacity of O_2, η is the dynamic viscosity of O_2, κ_{O_2} is the thermal conductivity of O_2, and ν is the kinematic viscosity of O_2. The temperature- and pressure-dependent properties of O_2 gas are obtained from the open literature [29–32].

Using Eqs. (12)-(16) and the properties of each alloy and of the O_2 gas, we calculate the heat dissipation rate from the rubbing surface during frictional ignition of each material. Fig. 19 shows these results as well as the individual contributions from conduction, radiation, and convection during a frictional ignition experiment on M400 under PO_2 = 6.9 MPa. Fig. 19 also shows the magnitude of the heat dissipation rate at the interface calculated using the 3-D FEM, indicated by the blue curve. The heat dissipation rate estimated using the analytical expressions in Eqs. (12)-(16), which assumed 1-D heat transfer, is in good agreement with that calculated using finite element simulations. In Fig. 19 the heat dissipation rate increases with time, consistent with the monotonic increase in interfacial temperature. We also observe that during frictional ignition experiments in O_2 gas, the main mechanism of heat dissipation from the rubbing surface is conduction along the sample length. The relative contributions of radiation, conduction, and convection to the overall heat dissipation rate are influenced by material chemistry, sample geometry, and test conditions. For example, substituting O_2 gas with a fluid possessing a higher heat transfer coefficient, such as liquid oxygen, will augment convective heat dissipation.

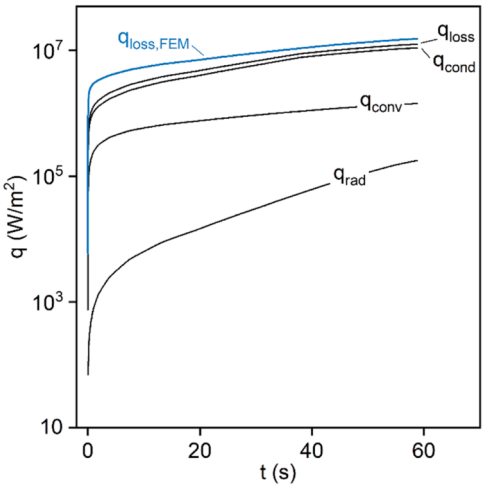

Fig. 19. Total heat dissipation rate (q_{loss}) from the rubbing interface, including the contributions of conduction (q_{cond}), convection (q_{conv}), and radiation (q_{rad}), during frictional ignition testing of M400 under PO_2 = 6.9 MPa. Blue curve indicates the heat dissipation rate calculated using FEM.

6. Application of the thermal ignition criterion to frictional ignition

In this section, we apply the frictional ignition criterion established above by comparing the heat dissipation rate and the oxidation heating rate, both with and without the presence of an oxide tribolayer, for each material in this study. These results highlight the underlying ignition mechanism for each material under a given set of test conditions and reveal why some materials exhibit different ignition mechanisms (melt-driven vs. solid-state mechanically-driven ignition) depending on the operating conditions.

6.1. Ni-Cu alloys

6.1.1. Monel 400

Fig. 20 shows the ignition criterion for M400 under PO_2 = 6.9 MPa. The heating rates from oxidation, both in the absence ($q_{ox,ad}$) and presence ($q_{ox,diff}$) of the tribolayer, and the total heat dissipation rate (q_{loss}), are plotted as functions of time in Fig. 20a. The broken line indicates when the heat flux from oxidation in the absence of the tribolayer is greater than the heat dissipation rate, i.e., when the thermal ignition criterion is satisfied. Fig. 20b shows the interfacial temperature as a function of time. The black horizontal line indicates the critical temperature (T^*) at which the thermal ignition condition is satisfied in

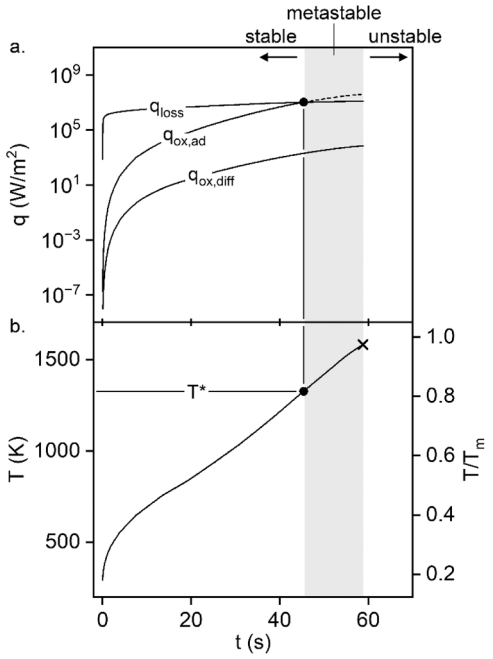

Fig. 20. Ignition criterion for M400 under $PO_2 = 6.9$ MPa. (a) Heat dissipation rate q_{loss}, and heating rates from oxidation in the absence of a tribolayer ($q_{ox,ad}$) and when a tribolayer forms ($q_{ox,diff}$) as a function of time. (b) Interfacial temperature vs. time. Black horizontal line indicates the critical temperature (T^*) and the cross indicates when ignition occurred.

the absence of an oxide tribolayer. Both $q_{ox,ad}$ and $q_{ox,diff}$ increase during the test, consistent with the rapid rise in interfacial temperature due to frictional heating. Towards the end of the test, the heating rate from oxidation when a tribolayer forms ($q_{ox,diff}$) is four orders of magnitude lower than when the tribolayer is absent ($q_{ox,ad}$).

Comparison of the heat dissipation rate with the heat generation rate (cf. Fig. 20a) reveals that when the oxide tribolayer is absent or insufficiently protective, the heat generation rate exceeds the heat dissipation rate ($q_{ox,ad} > q_{loss}$) at 45 s, corresponding to a critical temperature of 1330 K, cf. Fig. 20b. By contrast, when the oxide tribolayer forms, heat generation never surpasses the heat dissipation rate ($q_{ox,dif} < q_{loss}$), indicating that the formation of an oxide tribolayer effectively delays ignition. For ignition to occur, the tribolayer must break down, which happens when the interfacial temperature reaches the melting point of the Cu_2O phase in the oxide tribolayer. Tribolayer breakdown results in a jump in the heating rate, from $q_{ox,diff}$ to $q_{ox,ad}$. At this temperature, the heat generation rate exceeds the heat dissipation rate, satisfying the thermal ignition condition required for ignition.

Based on the results in Fig. 20, the ignition model accurately predicts melt-driven frictional ignition and suggests three temperature regimes: (i) a stable regime below the critical temperature; (ii) a metastable regime between the critical temperature and the ignition temperature, i.e., the interfacial temperature at which the tribolayer breaks down; and (iii) an unstable regime between the ignition temperature and the alloy melting point at which the protective tribolayer is guaranteed to break down. Ignition does not occur when the interfacial temperature is within the stable temperature window. When the interfacial temperature is within the metastable window, ignition may occur if the oxide tribolayer is disrupted. M400 has a narrow metastable temperature window due to its low enthalpy of oxidation, but it forms a relatively thin oxide tribolayer that is more susceptible to breakdown compared to tribolayers on other alloys that also ignite via a melt-driven mechanism, such as H214 and Ni-20Cr.

Eqs. (8), (11), and (12) link material chemistry and operating conditions with the heat dissipation rate (q_{loss}) and the oxidation heating rate (q_{ox}). In turn, these heat fluxes affect the ignition resistance through the critical temperature (T^*). Higher ignition resistance is achieved by increasing T^*, either by decreasing q_{ox} or increasing q_{loss} through adjustments in material properties, component geometry, and operating conditions. According to Eq. (6), the only means to reduce the heating rate from oxidation is by manipulating the material properties, specifically by decreasing either the oxidation rate (dm_c/dt) or the enthalpy of oxidation (H_{ox}). Similarly, increasing the heat dissipation rate and thus the critical temperature can be accomplished by increasing the thermal conductivity of the material. Previous frictional ignition and promoted combustion studies have alluded to these material property effects, suggesting that metals with low enthalpies of oxidation and high thermal conductivities are more ignition- and burn-resistant [1,2,37,51]. The present analysis provides a quantitative explanation of these effects, highlighting how tailoring material properties can improve ignition resistance.

Another approach for increasing the critical temperature is to enhance the dissipative heat flux by modifying component geometry or by manipulating the operating conditions. As one example, optimizing the contact area at the sliding interface can enhance heat dissipation through conduction while simultaneously reducing frictional heating by decreasing the contact pressure. As another example, the heat transfer coefficient can be manipulated using coolants. For instance, bearings in rocket engine turbomachinery are flooded with liquid coolants that have a high heat transfer coefficient to minimize frictional heating. Ignition of oxygen-flooded bearings has been linked to coolant boiling [52,53], corresponding to a drop in the heat transfer coefficient, lowering the critical temperature.

Adjusting the oxygen pressure can also increase the critical temperature and improve ignition resistance. However, the impact of PO_2 on ignition resistance is complex because it influences both oxidation kinetics and the cooling behavior. Higher O_2 pressures may accelerate oxidation kinetics, increasing the heating rate from oxidation and reducing the critical temperature. Concurrently, a higher PO_2 enhances the rate of heat dissipation into the gas via convection, increasing the critical temperature. The net effect on the ignition resistance of the system depends on the relative sensitivity of oxidation kinetics and the convective heat transfer coefficient to O_2 pressure. For example, the ignition mechanism of M400 is insensitive to PO_2, but the ignition time is delayed under a higher PO_2, indicating that for M400 the heat transfer coefficient is more sensitive to PO_2 than oxidation kinetics.

6.1.2. Toughmet 160

Fig. 21 shows the ignition criterion for TS160 under PO_2 of 6.9 MPa. The oxidative heat fluxes shown in Fig. 21a increase with time as in the case of M400. By the end of the test, $q_{ox,diff}$ is three orders of magnitude lower than $q_{ox,ad}$, reflecting the effects of tribolayer growth on oxidation kinetics. The oxidative heat flux in the presence of a tribolayer never surpasses the heat dissipation rate. Once the surface temperature reaches the melting point of TS160, the underlying metal melts, disrupting the oxide tribolayer and causing a jump in the heating rate from $q_{ox,diff}$ to $q_{ox,ad}$. At this temperature, the heating rate from oxidation exceeds the heat dissipation rate, satisfying the thermal ignition condition and ignition occurs. If the oxide tribolayer is absent, the oxidative heat flux exceeds the heat dissipation rate at 33 s, corresponding to a critical temperature of 1100 K, which is only 100 K lower than the ignition temperature (see Fig. 21b). The high critical temperature relative to its melting point indicates that TS160, despite forming a relatively weak oxide tribolayer, has a small unstable temperature window due to its low enthalpy of oxidation (185 kJ/mol) and high thermal conductivity (38 $Wm^{-1}K^{-1}$). Nonetheless, the potential of TS160 as an ignition-resistant material is limited by its low melting point, which can potentially be increased through judicious alloying modifications.

6.2. Haynes 214

Fig. 22 shows the ignition criterion for H214 under PO_2 of 6.9 MPa.

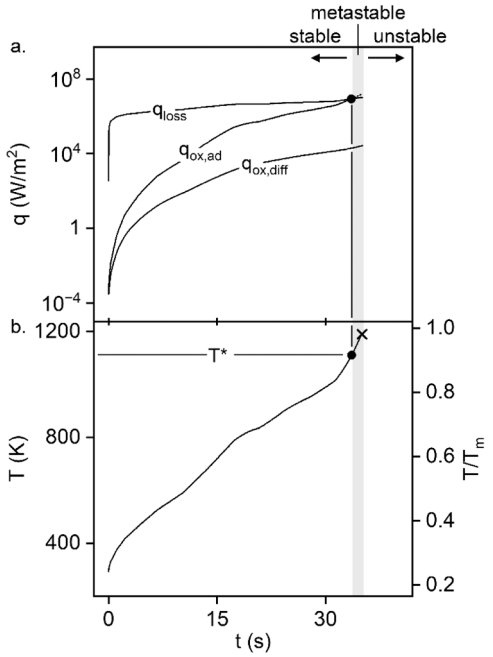

Fig. 21. Ignition criterion for TS160 under $PO_2 = 6.9$ MPa. (a) Heat dissipation rate q_{loss}, and heating rates from oxidation in the absence of a tribolayer ($q_{ox,ad}$) and when a tribolayer forms ($q_{ox,diff}$) as a function of time. (b) Interfacial temperature vs. time. Black horizontal line indicates the critical temperature (T^*) and the cross indicates when ignition occurred.

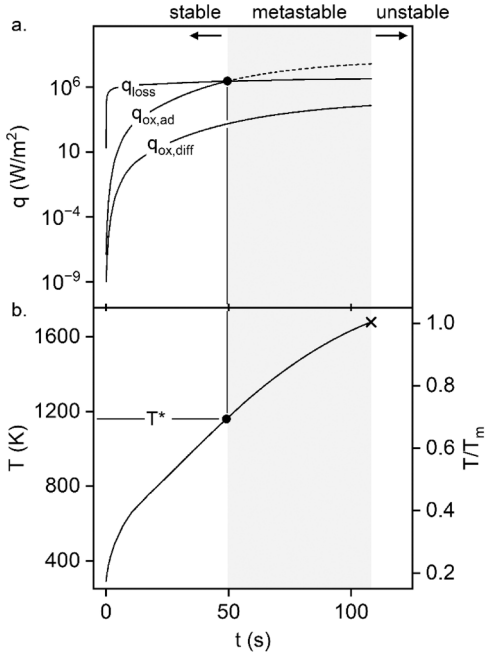

Fig. 22. Ignition criterion for H214 under $PO_2 = 6.9$ MPa. (a) Heat dissipation rate q_{loss}, and heating rates due to oxidation in the absence of a tribolayer ($q_{ox,ad}$) and when a tribolayer forms ($q_{ox,diff}$) as a function of time. (b) Interfacial temperature vs. time. Black horizontal line indicates the critical temperature (T^*) and the cross indicates when ignition occurred.

As in M400 and TS160, the growth of the tribolayer effectively mitigates ignition because the heating rate from oxidation never surpasses the heat dissipation rate when a tribolayer forms (see Fig. 22a). Once the surface temperature reaches the ignition temperature, which corresponds to the melting point of the alloy, the tribolayer breaks down and the heating rate from oxidation sharply increases ~3 orders of magnitude to $q_{ox,ad}$. At this point, the heating rate from oxidation is greater than the heat dissipation rate and ignition sets on. When the oxide tribolayer does not form during sliding, the heating rate from oxidation exceeds the heat dissipation rate at 55 s ($T^* = 1170$ K, cf. Fig. 22b). The critical temperature of H214 is 500 K lower than the ignition temperature, indicating that H214 has a wide metastable temperature window, and thus its ignition behavior depends strongly on the stability of its oxide tribolayer. A similar metastable regime is expected in Ni-20Cr and other Ni-Cr alloys due to the similarities in their ignition and sliding behaviors. As seen in Section 3.2, H214 and Ni-20Cr can resist ignition only when they form thick, adherent oxide tribolayers, which is more likely under higher O_2 pressures.

The ignition resistance of H214 can be improved by increasing T^*, using the same strategies for M400 discussed in Section 6.1.1. However, compared to M400, adjusting the oxygen pressure has a different net effect on the ignition resistance of H214 and Ni-20Cr. For example, we observed that the ignition mechanism of H214 and Ni-20Cr transitions from melt-driven ignition under a higher PO_2 to solid-state mechanically-driven ignition under a lower PO_2. This transition occurs because oxidation kinetics in H214 and Ni-20Cr are more sensitive to PO_2 than the heat transfer coefficient, resulting in the growth of a thin oxide tribolayer that is susceptible to mechanical breakdown under lower PO_2. And while under a lower PO_2, the critical temperature may rise due to slower oxidation kinetics, the resulting thin tribolayers on H214 and Ni-20Cr can more easily break down, triggering metal ignition at a lower surface temperature and a lower contact pressure.

In addition to the above strategies to increase the ignition resistance of the sliding system, ignition can also be suppressed by enhancing the mechanical stability of the tribolayer, ensuring that the tribolayer does not fail and the system is unlikely to ignite. A thick, protective tribolayer offers two main advantages – it lubricates the sliding surface, thereby lowering the friction coefficient and reducing frictional heating, and it protects against further oxidation, slowing oxidation kinetics and decreasing the heating rate from oxidation (cf. Fig. 22). In our past work we observed that to achieve a thick and adherent tribolayer, specific properties of the tribolayer and parent metal are desirable. The alloy must rapidly grow a thick, adherent oxide tribolayer [9]. Developing a tribolayer with a fine grained structure can help accelerate oxide growth through short-circuit diffusion along grain boundaries [26,27]. Tribolayer adhesion can be improved by growing oxide interlayers such as Cr_2O_3 or Al_2O_3 at the metal/oxide interface, and by enhancing the interfacial toughness of the metal/oxide interface through oxide pegs and corrugations [54–58]. Additionally, both the oxide and underlying metal must retain their strength at elevated temperatures to minimize plastic deformation. This can be achieved through the formation of refractory oxide precipitates such as $NiCr_2O_4$ in the tribolayer, which strengthen the tribolayer, and by incorporating oxide dispersoids in the alloy to strengthen the underlying metal [9]. An exemplary material that exhibits these properties is Inconel MA754, an oxide dispersion-strengthened Ni-Cr alloy that possesses exceptional frictional ignition resistance due to the unique properties of its thick, adherent oxide tribolayer [9].

7. Generalization of the ignition criterion to other alloys

We conclude by expanding our analysis to other materials assessed in our previous study [9] and in previous work by NASA WSTF [1,2], determining their critical temperature T^*, i.e., the interfacial temperature at which an alloy can ignite in the absence of a protective oxide tribolayer. Using the same approach described in Section 5 we determined the critical temperature for each alloy. Fig. 23 compares the ignition and critical temperatures of each alloy, assuming $PO_2 = 6.9$ MPa. For all materials the critical temperature is lower than the ignition temperature, indicating that the thermal ignition condition was satisfied when frictional ignition occurred. This strong agreement

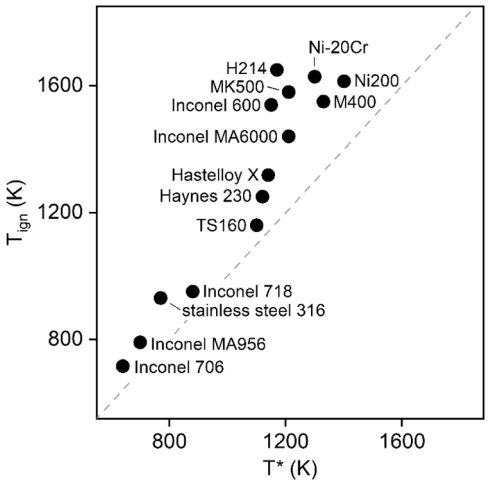

Fig. 23. Ignition temperature of the alloy (T_{ign}) calculated using the FEM vs. critical temperature (T^*) calculated using the ignition model under PO_2 = 6.9 MPa. Frictional ignition data used to calculate T_{ign} and T^* was retrieved from [1,2].

provides confidence that the ignition model can accurately predict critical conditions resulting in ignition. Interestingly, materials that ignite at a lower temperature have a critical temperature close to their ignition temperature. For example, Inconel 718, stainless steel 316, and Inconel 706 have critical temperatures of 880 K, 770 K, and 640 K, respectively, only 70 K, 160 K, and 80 K lower than their ignition temperatures, which were 950 K, 930 K, and 710 K, respectively. An ignition temperature close to the critical temperature suggests that these materials form thin, weak oxide tribolayers. Conversely, Ni-20Cr, H214, and Inconel 600 have critical temperatures of 1210 K, 1300 K, and 1170 K, well below their ignition temperatures of 1580 K, 1630 K, and 1650 K, respectively, indicating that these materials grow a thick, adherent oxide tribolayer that successfully mitigates frictional ignition.

Fig. 24 compares the three temperature regimes established in Section 6.1.1 by plotting the critical temperature and ignition temperature under a PO_2 of 6.9 MPa as well as the melting point of each alloy. Among the materials assessed in this study, TS160 has the smallest metastable temperature window. Its critical temperature is close to the melting point, indicating that the growth of a thick and adherent oxide tribolayer is not necessary for mitigating ignition in TS160. M400 and Ni200, both of which form relatively thin oxide tribolayers compared to other ignition-resistant materials, have critical temperatures close to their melting points and a small metastable temperature window. Their

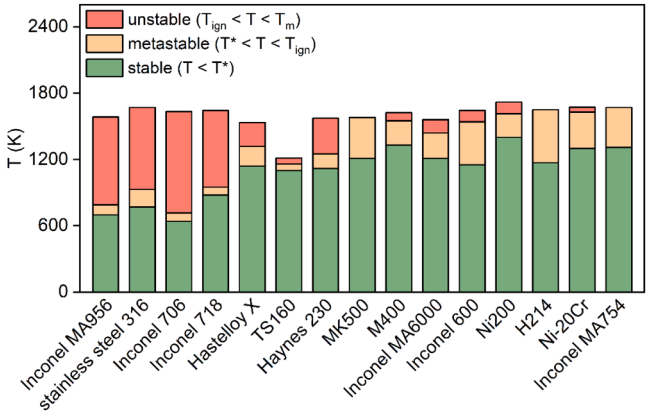

Fig. 24. Comparison of the critical temperature (T^*), ignition temperature (T_{ign}), and the melting point (T_m) of each alloy. Frictional ignition data used to calculate T^* and T_{ign} was retrieved from [1,2].

ignition resistance can be improved through a combination of strategies that push the critical temperature even closer to the melting point, as discussed in Section 6.1.1. H214 and Ni-20Cr, despite having a relatively low critical temperature, ignite at a higher temperature close to their melting point due to the formation of thick, adherent oxide tribolayers. For these alloys, the main approach to mitigating frictional ignition is to enhance tribolayer stability via material chemistry adjustments as described in Section 6.2. By contrast, Inconel 706, Inconel MA956, Inconel 718, and stainless steel 316 have low critical temperatures and a small metastable temperature window. For these materials, frictional ignition may be mitigated by combining strategies to increase the critical temperature and to promote the formation of a thick, adherent oxide tribolayer.

Based on the above observations, it is evident that materials with a critical temperature close to their melting point (i.e., materials that have small metastable and small unstable regimes such as TS160, M400, and Ni200) likely ignite via a melt-driven mechanism. By contrast, alloys with a critical temperature well below their melting point may exhibit melt-driven ignition under favorable conditions that result in a large metastable temperature window (e.g., H214 and Ni-20Cr under high PO_2). However, these materials are more prone to solid-state mechanically-driven ignition because their ignition resistance depends on the stability of their oxide tribolayer.

8. Conclusions

High-speed sliding experiments under high-pressure gaseous O_2 were used to assess the frictional ignition behaviors of Monel K500, Monel 400, Toughmet 160, and Haynes 214. All materials exhibited a decay in the friction coefficient due to the growth of an oxide tribolayer during sliding. The phase distribution observed in the tribolayer aligns well with that predicted using equilibrium thermochemical calculations indicating that such calculations can be used to predict the oxide phases in tribolayers. Frictional ignition was directly linked to tribolayer breakdown, which exposed the hot underlying metal to high O_2 pressure and triggered ignition.

We identified three distinct tribolayer breakdown mechanisms that drive frictional ignition: (i) melting of the oxide tribolayer; (ii) melting of the underlying metal; and (iii) solid-state mechanically-driven failure. Haynes 214 exhibited two different ignition mechanisms depending on the test conditions – melting of the underlying metal under an O_2 pressure of 6.9 MPa and mechanical failure under an O_2 pressure of 3.4 MPa.

Using thermal ignition theory, we determined a critical interfacial temperature above which a material can ignite in the absence of an oxide tribolayer. This temperature is typically well below the observed ignition temperature and the melting point, suggesting three regimes of interfacial temperature: (i) a stable regime below the critical temperature; (ii) a metastable regime between the critical and ignition temperature, i.e., the surface temperature at which the tribolayer breaks down; and (iii) an unstable regime between the ignition temperature and the alloy melting point. In the metastable regime, ignition occurs if the protective oxide tribolayer breaks down. The critical temperature provides a conservative bound for designing against frictional ignition.

Of the materials tested, the critical temperature of Toughmet 160 is the closest to its melting point due to its high thermal conductivity and low enthalpy of oxidation. Monel 400 develops a tribolayer that is prone to breakdown, but it has a relatively high critical temperature because of its low enthalpy of oxidation. Ni-20Cr and Haynes 214 have a wide metastable temperature window within which their ignition behavior depends on the stability of their oxide tribolayer. Ignition is mitigated only when they form a thick, adherent oxide tribolayer.

We extended our analysis to other materials and observed that alloys with a critical temperature close to their melting point likely ignite via a melt-driven mechanism. By contrast, alloys with a critical temperature well below their melting point may exhibit melt-driven ignition under

favorable conditions but can also exhibit solid-state mechanically-driven ignition. This analysis suggests two strategies for improving frictional ignition resistance. The first is to increase the critical temperature towards the alloy melting point by either decreasing the heating rate from oxidation or increasing the heat dissipation rate from the interface. The heating rate from oxidation can be reduced by adjusting material chemistry to lower the enthalpy of oxidation. The heat dissipation rate may be increased by optimizing component geometry, manipulating operating conditions, or tailoring chemistry to enhance the thermal conductivity of the material. The other strategy is to tailor alloy chemistry to promote the growth of a thick, adherent tribolayer that is less susceptible to breakdown so that the material can safely operate in the metastable regime.

CRediT authorship contribution statement

Andres Garcia Jimenez: Writing – original draft, Methodology, Investigation, Conceptualization. **Timothy Wabel:** Methodology, Investigation. **Fabio A. Bendana:** Writing – review & editing, Methodology, Investigation. **John D. DeSain:** Methodology, Investigation. **Levon Gevorkyan:** Resources, Methodology. **Zachary C. Cordero:** Writing – review & editing, Supervision, Methodology, Conceptualization.

Declaration of Competing Interest

The authors declare that they have no known competing financial interests or personal relationships that could have appeared to influence the work reported in this paper.

Acknowledgments

This research was enabled by financial support from the NSF through grants DMR-2004913 and the Space Systems Command (SSC) under contract FA8802-19-C-0001. A.G.J. gratefully acknowledges support from the NSF Graduate Research Fellowship Program through grant No. 2141064. We thank Dr. Andrew Cortopassi, Dr. Vincent Phong, Armando Perezselsky, and Devon Smith from The Aerospace Corporation for their support with the frictional ignition tests. The authors are also thankful for the ongoing programmatic support of John Di Pol and Dr. James Morehart at The Aerospace Corporation.

Data availability

Data will be made available on request.

References

[1] Stoltzfus JM, Benz FJ, Homa J. The Pv product required for the frictional ignition of alloys, 4. Las Cruces, NM: ASTM International; 1989. p. 212–27.
[2] Benz FJ, Stoltzfus JM. Ignition of metals and alloys in gaseous oxygen by frictional heating. Flammabl. sensit. mater. oxyg.-enriched atmospheres second vol. ASTM International; 1986. p. 38–58. https://doi.org/10.1520/STP19308S.
[3] Stoltzfus JM, Gunaji MV. Test methods for determining the suitability of metal alloys for use in oxygen-enriched environments, 1. ASTM International; 1991. p. 183–92.
[4] Garcia Jimenez A, Cordero ZC. Frictional ignition of metals in high pressure oxygen: a critical reassessment of NASA test data. Am Inst Aeronaut Astronaut 2023:1489. https://doi.org/10.2514/6.2023-1489.
[5] Breiter AL, Mal'tsev VM, Popov EI. Models of metal ignition. Combust Explos Shock Waves 1977;13:475–85. https://doi.org/10.1007/BF00744795.
[6] Abbud-Madrid A, Fiechtner GJ, Branch MC, Daily JW. Ignition and combustion characteristics of pure bulk metals: normal-gravity test results. Reno, NV 1994.
[7] Jones PD. Flammability of heterogeneously combusting metals. Inorg. Phys. Chem. Marshall Space Flight Center; 1998.
[8] Markstein GH. Heterogeneous reaction processes in metal combustion. Symp Int Combust 1967;11:219–34. https://doi.org/10.1016/S0082-0784(67)80149-8.
[9] Jimenez AG, Wabel T, Bendana FA, DeSain JD, Xu M, LeBeau JM, et al. Frictional ignition of dispersion-strengthened Ni-Cr alloys. Tribol Int 2024:109370. https://doi.org/10.1016/j.triboint.2024.109370.
[10] Glassman I, Yetter RA, Glumac NG. Combustion. 5th ed. Academic Press; 2014.
[11] Semenov NN. Chemical kinetics and chain reactions, 12. London: Oxford: Clarendon Pres; 1935.
[12] Semenov N.N., Thermal theory of combustion and explosion. NACA-TM-1026. Langley Research Center, 1942.
[13] Mikkola E, Wichman IS. On the thermal ignition of combustible materials. Fire Mater 1989;14:87–96. https://doi.org/10.1002/fam.810140303.
[14] Gevorkyan L, McCall S, Smolke J, Driscoll R. A test apparatus for the characterization of ignitability and flammability of metals in high pressure oxygen. Propuls. Energy 2019 Forum. Indianapolis, IN: American Institute of Aeronautics and Astronautics; 2019. https://doi.org/10.2514/6.2019-4351.
[15] Wabel TM, Bendana F, DeSain J, Gevorkyan L. Friction ignition testing of metals in oxygen up to 24.1 MPa. American Institute of Aeronautics and Astronautics; 2023. p. 1491. https://doi.org/10.2514/6.2023-1491.
[16] Standard Guide for Cleanliness Levels and Cleaning Methods for Materials and Equipment Used in Oxygen-Enriched Environments, 2019.
[17] Bale C.W., Belisle E., Chartrand P., Decterov S.A., Eriksson G., Gheribi A.E., et al. FactSage Thermochemical Software and Databases 2010.
[18] COMSOL Multiphysics® v. 6.2. ⟨www.comsol.com⟩. COMSOL AB, Stockholm, Sweden. 2024.
[19] Lewis FB, Saunders NH. The thermal conductivity of NiO and CoO at the Neel temperature. J Phys C Solid State Phys 1973;6:2525. https://doi.org/10.1088/0022-3719/6/15/012.
[20] Sahoo P, Misra DK, Salvador J, Makongo JPA, Chaubey GS, Takas NJ, et al. Microstructure and thermal conductivity of surfactant-free NiO nanostructures. J Solid State Chem 2012;190:29–35. https://doi.org/10.1016/j.jssc.2012.01.052.
[21] Linnera J, Karttunen AJ. Ab initio study of the lattice thermal conductivity of Cu2O using the generalized gradient approximation and hybrid density functional methods. Phys Rev B 2017;96:014304. https://doi.org/10.1103/PhysRevB.96.014304.
[22] Haugsrud R. High-temperature oxidation of Ni–20 wt% Cu from 700 to 1100°C. Oxid Met 2001;55:571–83. https://doi.org/10.1023/A:1010368017367.
[23] Haugsrud R, Kofstad P. On the high-temperature oxidation of Cu-Rich Cu-Ni alloys. Oxid Met 1998;50:189–213. https://doi.org/10.1023/A:1018884120304.
[24] Pilling NB, Bedworth RE. Oxidation of copper-nickel alloys at high temperatures. Ind Eng Chem 1925;17:372–6. https://doi.org/10.1021/ie50184a013.
[25] Chattopadhyay B, Wood GC. The transient oxidation of alloys. Oxid Met 1970;2:373–99. https://doi.org/10.1007/BF00604477.
[26] Atkinson A. Wagner theory and short circuit diffusion. Mater Sci Technol 1988;4:1046–51. https://doi.org/10.1179/mst.1988.4.12.1046.
[27] Herchl R, Khoi NN, Homma T, Smeltzer WW. Short-circuit diffusion in the growth of nickel oxide scales on nickel crystal faces. Oxid Met 1972;4:35–49. https://doi.org/10.1007/BF00612506.
[28] Atkinson HV. A review of the role of short-circuit diffusion in the oxidation of nickel, chromium, and nickel-chromium alloys. Oxid Met 1985;24:177–97. https://doi.org/10.1007/BF00664231.
[29] Stewart RB, Jacobsen RT, Wagner W. Thermodynamic properties of oxygen from the triple point to 300 K with pressures to 80 MPa. J Phys Chem Ref Data 1991;20:917–1021. https://doi.org/10.1063/1.555897.
[30] Lemmon EW, Jacobsen RT. Viscosity and thermal conductivity equations for nitrogen, oxygen, argon, and air. Int J Thermophys 2004;25:21–69. https://doi.org/10.1023/B:IJOT.0000022327.04529.f3.
[31] McBride BJ, Zehe MJ, Gordon S. NASA glenn coefficients for calculating thermodynamic properties of individual species. Glenn Research Center: NASA; 2002.
[32] Air Products and Chemicals Inc. Thermodynamic data on oxygen and nitrogen. Wright-Patterson Air Force Base OH: 1961.
[33] Stott FH, Wood GC, Hobby MG. A comparison of the oxidation behavior of Fe-Cr-Al, Ni-Cr-Al, and Co-Cr-Al alloys. Oxid Met 1971;3:103–13. https://doi.org/10.1007/BF00603481.
[34] Kvernes IA, Kofstad P. The oxidation behavior of some Ni-Cr-Al alloys at high temperatures. Met Trans 1972;3:1511–9. https://doi.org/10.1007/BF02643040.
[35] Giggins CS, Pettit FS. Oxidation of Ni - Cr - Al alloys between 1000° and 1200°C. J Electrochem Soc 1971;118:1782. https://doi.org/10.1149/1.2407837.
[36] Reynolds WC. Investigation of ignition temperatures of solid metals. Stanford Univ., Calif.; 1959.
[37] McIlroy K, Zawierucha R, Drnevich RF. Promoted ignition behavior of engineering alloys in high-pressure oxygen. Flammabl. sensit. mater. oxyg.-enriched atmospheres, 3. ASTM International; 1988. p. 85–104. https://doi.org/10.1520/STP26741S.
[38] Lynn D, Steinberg T, Sparks K, Stoltzfus J. Defining the flammability of cylindrical metal rods through characterization of the thermal effects of the ignition promoter. J ASTM Int 2009;6:JAI102253. https://doi.org/10.1520/JAI102253.
[39] Quinn TFJ. Oxidational wear modelling: I. Wear 1992;153:179–200. https://doi.org/10.1016/0043-1648(92)90269-E.
[40] Quinn TFJ. Oxidational wear modelling: Part II. The general theory of oxidational wear. Wear 1994;175:199–208. https://doi.org/10.1016/0043-1648(94)90183-X.
[41] Quinn TFJ. Oxidational wear modelling Part III. The effects of speed and elevated temperatures. Wear 1998;216:262–75. https://doi.org/10.1016/S0043-1648(98)00137-9.
[42] Allen CB, Quinn TFJ, Sullivan JL. The oxidational wear of high-chromium ferritic steel on austenitic stainless steel. J Tribol 1985;107:172–9. https://doi.org/10.1115/1.3261016.
[43] Sullivan JL, Quinn TFJ, Rowson DM. Developments in the oxidational theory of mild wear. Tribol Int 1980;13:153–8. https://doi.org/10.1016/0301-679X(80)90031-6.

[44] Taylor HS. The activation energy of adsorption processes. J Am Chem Soc 1931;53:578–97. https://doi.org/10.1021/ja01353a022.
[45] Canning NDS, Outka D, Madix RJ. The adsorption of oxygen on gold. Surf Sci 1984;141:240–54. https://doi.org/10.1016/0039-6028(84)90209-7.
[46] Lanyon M a H, Trapnell BMW, Hinshelwood CN. The interaction of oxygen with clean metal surfaces. Proc R Soc Lond Ser Math Phys Sci 1997;227:387–99. https://doi.org/10.1098/rspa.1955.0018.
[47] Bonzel HP, Ku R. On the kinetics of oxygen adsorption on a Pt(111) surface. Surf Sci 1973;40:85–101. https://doi.org/10.1016/0039-6028(73)90053-8.
[48] Hertz H. Ueber die Verdunstung der Flüssigkeiten, insbesondere des Quecksilbers im luftleeren Raume. J Phys Théorique Appliquée 1882;1:512–3. https://doi.org/10.1051/jphystap:018820010051200.
[49] Knudsen M. Die maximale Verdampfungsgeschwindigkeit des Quecksilbers. Ann Phys 1915;352:697–708. https://doi.org/10.1002/andp.19153521306.
[50] Anderson JT, Saunders OA, Taylor GI. Convection from an isolated heated horizontal cylinder rotating about its axis. Proc R Soc Lond Ser Math Phys Sci 1997;217:555–62. https://doi.org/10.1098/rspa.1953.0080.
[51] Zawierucha R., Ilroy K.M. Promoted Ignition - Combustion Behavior of Selected Engineering Alloys In Oxygen Gas Mixtures. Flammabl. Sensit. Mater. Oxyg.-Enriched Atmospheres, vol. 4, ASTM International; n.d., p. 145–161. https://doi.org/10.1520/STP24925S.
[52] Gibson HG. Design guide for bearings used in cryogenic turbopumps and test rigs. M-1496. Marshall Space Flight Center: NASA NTRS; 2019.
[53] Bond J. Sources of ignition: flammability characteristics of chemicals and products. Oxford: Elsevier; 2017.
[54] Li BW, Zhao HP, Qin QH, Feng XQ, Yu SW. Numerical study on the effects of hierarchical wavy interface morphology on fracture toughness. Comput Mater Sci 2012;57:14–22. https://doi.org/10.1016/j.commatsci.2011.01.032.
[55] Sehr S, Amidi S, Begley MR. Interface delamination vs. bulk cracking along wavy interfaces. Eng Fract Mech 2019;206:64–74. https://doi.org/10.1016/j.engfracmech.2018.10.031.
[56] Alexander KB, Prusner K, Pint BA, Tortorelli PF. The effect of reactive-element alloying additions on the microstructure and microchemistry of thermally-grown oxide scales on nickel-based alloys. Energy 1998;12:16.
[57] Stringer J, Wilcox BA, Jaffee RI. The high-temperature oxidation of nickel-20 wt% chromium alloys containing dispersed oxide phases. Oxid Met 1972;5:11–47. https://doi.org/10.1007/BF00614617.
[58] Wright IG, Wilcox BA, Jaffee RI. The high-temperature oxidation of Ni-20%Cr alloys containing various oxide dispersions. Oxid Met 1975;9:275–305. https://doi.org/10.1007/BF00613277.